LHCb-CONF-2013-007
April 19, 2013

Measurement of the cross-section for $Z \to \mu^+\mu^-$ production with 1 fb^{-1} of pp collisions at $\sqrt{s}$=7 TeV

The LHCb collaboration [†]

Abstract

A measurement of the cross-section for $Z \to \mu\mu$ is presented using LHCb data recorded in 2011. The cross-section is measured for muons with a transverse momentum larger than 20 GeV/c in the pseudorapidity range $2.0 < \eta < 4.5$. The invariant mass of the dimuon system is restricted to $60 < M < 120$ GeV/c^2. The cross-section is also measured differentially as a function of the rapidity, transverse momentum and ϕ^* of the Z boson.

[†]Conference report prepared for the DIS 2013 workshop on deep inelastic scattering and related subjects, april 2013. Contact authors: Jonathan Anderson and Ronan Wallace (jonathan.anderson@cern.ch, ronan.wallace@cern.ch)

1 Introduction

The measurement of vector boson production in LHCb permits a number of tests of electroweak and QCD predictions. The kinematic range of LHCb, about $2 < \eta < 5$ in pseudorapidity, complements that of the general purpose detectors ATLAS and CMS, with a small region of overlap. Measurements at LHCb are sensitive to the proton structure functions at very low values of Bjorken x, where the parton distribution functions (PDFs) are not well constrained by previous data from HERA. LHCb has published measurements of Z production[1] for the decay into two muons [1], electrons [2] and tau leptons [3]. W production has been measured in the muon channel [1]. This analysis supersedes the previous measurement in the muon channel. It is based on data collected in 2011, corresponding to an integrated luminosity of about 1 fb^{-1}, which is 30 times more than the published analysis. Since the systematic uncertainties are mostly statistical in nature, the total uncertainty of the measurement is significantly reduced. The measurement is performed for muons with transverse momenta $p_{\rm T}^{\mu} > 20$ GeV/c, and $2.0 < \eta < 4.5$. The invariant mass of the two muons is required to be in the range $60 < M_{\mu\mu} < 120\,{\rm GeV}/c^2$. Results are presented as differential cross-sections as a function of the rapidity (y), transverse momentum ($p_{\rm T}$) and ϕ^* of the Z boson, where ϕ^* is defined as

$$\phi^* = \tan(\phi_{\rm acop}/2)/\cosh(\Delta\eta/2),$$

where $\phi_{\rm acop} = \pi - |\Delta\phi|$ depends on the azimuthal difference of the two muons [4]. ϕ^* is correlated to $p_{\rm T}/M_{\mu\mu}$ and therefore probes the same physics as $p_{\rm T}$ of the Z boson. Since in general the angles are better measured than the momentum of the particle, ϕ^* is better determined than the $p_{\rm T}$ of the Z boson.

The remainder of this note is organised as follows: Sect. 2 describes the detector, Sect. 3 describes the triggers, datasets and the selection of the sample; Sect. 4 explains the efficiencies and corrections for acceptance and final state radiation and the systematic uncertainties; Sect. 5 presents the results.

2 LHCb detector

The LHCb detector [5] is a single-arm forward spectrometer covering the pseudorapdity range $2 < \eta < 5$, designed for the study of particles containing b or c quarks. The detector includes a high precision tracking system consisting of a silicon-strip vertex detector (VELO) surrounding the pp interaction region, a large-area silicon-strip detector (TT) located upstream of a dipole magnet with a bending power of about 4 Tm, and three stations of silicon-strip detectors (IT) and straw drift-tubes (OT) placed downstream. The combined tracking system has a momentum resolution $\Delta p/p$ that varies from 0.4% at 5 GeV/c to 0.6% at 100 GeV/c, and an impact parameter resolution of 20 µm for tracks with high transverse momentum. Charged hadrons are identified using two ring-imaging Cherenkov detectors. Photon, electron and hadron candidates are identified by a calorimeter system

[1]Throughout this paper Z includes both the Z and the virtual photon ($\gamma^\star$) contribution.

consisting of scintillating-pad and pre-shower detectors, an electromagnetic calorimeter and a hadronic calorimeter. Muons are identified by a muon system composed of alternating layers of iron and multiwire proportional chambers. The trigger consists of a hardware stage, based on information from the calorimeter and muon systems, followed by a software stage which applies a full event reconstruction. To avoid the possibility that a few events with high occupancy dominate the CPU time of the software trigger, a set of global event cuts (GEC) is applied on the hit multiplicities of most subdetectors used in the pattern recognition algorithms.

3 Event selection

The analysis is based on the dataset collected in 2011. During this period the LHC collided protons with a centre-of-mass energy of 7 TeV. The data sample of this analysis corresponds to an integrated luminosity of about 1.0 fb^{-1}.

3.1 Simulation

The simulation of the signal and electroweak, top quark, and heavy flavour ($b\bar{b}$ and $c\bar{c}$ production) backgrounds has been performed using the Pythia 6.4 [6] generator, configured as described in Ref. [7], with the CTEQ6ll [8] parametrisation for the PDFs.

3.2 Selection and event yield

Events with two muons are selected using a single muon trigger which is efficient for muons with transverse momenta larger than 10 GeV/c. At least one of the muons is required to have passed this trigger line. Candidate events are selected by requiring a pair of well-reconstructed tracks of opposite charge identified as muons that combine to an invariant mass, $M_{\mu\mu}$, in the range $60 \leq M_{\mu\mu} \leq 120\,\text{GeV}/c^2$. Each muon track must have a transverse momentum $p_{\text{T}}^{\mu} > 20\,\text{GeV}/c$ and lie in the pseudorapidity range $2.0 \leq \eta \leq 4.5$. The relative error on the momentum measurement is required to be less than 10% and the χ^2 probability of the track fit must be larger than 0.1%. In total 52626 Z candidates are selected. Figure 1 shows the Z mass distribution for the selected events.

In order to understand possible systematic effects, approximately half of the analysed dataset was collected with the LHCb magnet polarity reversed, thus splitting the sample into magnet polarity "up" and magnet polarity "down" sub-samples.

3.3 Determination of sample purity

The background contribution to the selected $Z \to \mu\mu$ candidate sample is very low. Five different sources are investigated.

1. **Heavy flavour**: $b\bar{b}$ and $c\bar{c}$ production can contribute to the background if the resulting heavy flavour hadrons decay semileptonically. The contribution is estimated

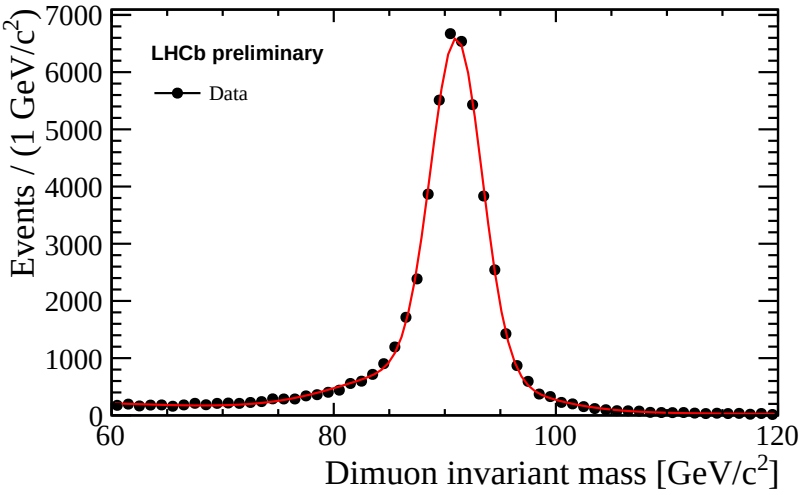

Figure 1: Invariant mass of the selected muon pairs. A double Gaussian function is fitted to the distribution.

from two independent samples that are enriched in background. The first sample is composed of events containing two muons with ${p_{\rm T}}^{\mu} > 15$ GeV/c, a dimuon invariant mass > 40 GeV/c, and a high probability that the two selected muons do not come from the same vertex. The second sample is composed of events that contain two muons that are poorly isolated with respect to the rest of the event and have ${p_{\rm T}}^{\mu} > 15$ GeV/c and a dimuon invariant mass > 40 GeV/c. Here the muon isolation is defined as the fraction of the transverse momentum of the muon-jet carried by the muon, $z = {p_{\rm T}}^{\mu}/{p_{\rm T}}^{\mu-jet}$, where the muon-jet is defined as the jet that contains the muon. The jet is reconstructed with the anti-kt [9] algorithm with the size $R = \sqrt{\Delta\eta_{ij}^2 + \Delta\phi_{ij}^2} = 0.5$, where $\Delta\eta_{ij}$ and $\Delta\phi_{ij}$ give the separation of two particles in the jet in η and azimuthal angle ϕ. An exponential fit to both dimuon invariant mass distributions in the range $40 - 60$ GeV/c^2 is performed to estimate the background in the Z mass region $60 - 120$ GeV/c^2. The efficiency of the vertex fit χ^2 requirement on heavy flavour events is determined from data by applying it to the heavy flavour sample selected using the muon isolation requirement. The efficiency of the muon isolation cut can be determined in a similar way using the sample selected using the vertex fit χ^2 requirement. For this efficiency determination to work, the isolation of the final state muons and the vertex fit χ^2 of the dimuon candidate must be uncorrelated for heavy flavor events; this assumption has been verified using simulated $b\bar{b}$ and $c\bar{c}$ events. The background due to heavy flavour decays is estimated to be 93 ± 13 events, where the error reflects the uncertainty on the extrapolation and the efficiency of the enrichment cuts.

2. **Hadron mis-id**: Pions or kaons may be misidentified as muons if they decay in

flight before they reach the muon stations or if they have sufficient energy to traverse the calorimeters and be detected in the muon stations. This background should contribute equally in same-sign and opposite-sign combinations of the muon pair. 25 events with both tracks having the same charge are found by the Z selection. We therefore estimate the background contribution from this source to be 25 ± 5 events. This background estimate also includes a possible contribution from W production together with a misidentified muon.

3. $\boldsymbol{Z \rightarrow \tau\tau}$: The decay $Z \rightarrow \tau\tau$ can contribute if both tau leptons decay leptonically to muons and neutrinos. Using a Z cross-section that is fixed to the cross-section measured in this analysis, the tau background is estimated from PYTHIA simulation and contributes 16 ± 3 events to the total sample.

4. **Top quark**: Decays of top quark pairs may contribute if both top quarks decay semileptonically. PYTHIA simulation predicts a contribution of 14 ± 1 events.

5. **WW**: W pair production contributes to the sample if both W bosons decay to a muon and a neutrino. This contribution is estimated from PYTHIA simulation to be to 5 ± 1 events.

The total background contribution in the Z sample in the range $60 - 120$ GeV/c^2 amounts to 153 ± 14 events. This corresponds to a purity $\rho = 0.9971 \pm 0.0003$. The purity is defined as the ratio of signal to candidate events. As no evidence is found for a variation of the background contribution as a function of y, ϕ^* and p_{T} of the Z boson, the purity is assumed to be constant over the three variables.

4 Cross-section selection

4.1 Cross-section definition

Cross-sections are quoted in the kinematical range defined by the measurements. The cross-sections are measured in bins of y, p_{T} and ϕ^* of the Z boson. The cross-section in a given bin i is defined as

$$\sigma_{Z\rightarrow\mu\mu}(i) = \frac{\rho f_{\mathrm{FSR}(i)} f_{\mathrm{MGR}(i)}}{\mathcal{L}\mathcal{A}} \sum_k \frac{1}{\varepsilon(\eta_k^{\mu^+}, \eta_k^{\mu^-}, PV_k)} \tag{1}$$

where k indexes the events in bin i, $\varepsilon(\eta_k^{\mu^+}, \eta_k^{\mu^-}, PV_k)$ is the total efficiency for a given event, dependent on η of the two muons and the number of primary interactions and ρ is the purity of the sample. The acceptance ($\mathcal{A}$), the correction factors for FSR f_{FSR} and bin migrations f_{MGR} are determined per bin; $\mathcal{L}$ is the integrated luminosity. The total cross-section is obtained by summing the contributions of the y bins.

4.2 Signal efficiencies

The data are corrected for efficiency losses due to track reconstruction, muon identification, and trigger requirements. All efficiencies are determined from data.

The efficiencies for track reconstruction and muon identification are obtained using a tag-and-probe method with a Z sample. One of the muons in the Z sample (tag) satisfies all of the track, muon-id and trigger criteria. The other muon (probe) is selected with looser criteria that depend on the efficiency to be measured. The invariant mass of the dimuon candidates, reconstructed from the tag and the probe muons, must lie within $10\,\mathrm{GeV}/c^2$ of the nominal Z mass. The tracking efficiency, which accounts for track reconstruction and the track quality requirements, is studied using well reconstructed tracks in the muon stations that are linked to hits in TT [10]. The average track finding efficiency for both tracks of the Z is found to be 81.0%. The muon identification efficiency is determined with tracks without the muon identification requirement for the probe muon. The average identification efficiency for the two muons is 97.5%.

The trigger efficiency contains two components, the first due to the efficiency of the single muon trigger and the other due to the global event cuts (GEC). The single muon trigger efficiency is determined using a tag-and-probe approach and the $Z \to \mu\mu$ sample. One of the muons in the final state is required to fire the single muon trigger while the other muon is used to investigate the trigger efficiency. The average trigger efficiency for events in the sample is determined to be 94.6%

The requirement on the occupancy of the events has an efficiency that depends on the multiplicity of the primary interactions. The efficiency of these GECs is evaluated from data. The main effect comes from the requirement that there are no more than 600 hits in the SPD. The efficiency is studied as a function of the number of primary proton-proton interactions in the event using two independent methods. The first method simulates higher pile-up events by adding no bias events to Z events with one primary vertex. It was checked that no events are lost if there is only one primary vertex reconstructed using a data sample that was collected with no GECs applied. The second method uses a fit to the SPD hit distribution in a sample triggered by the di-muon trigger with a higher cut on the number of SPD hits to estimate the efficiency. Both methods give consistent measurements of the GEC efficiency, and the second method is taken for the analysis; the uncertainty of the fit is added to the systematic uncertainty of the trigger efficiency. An average efficiency of 95.9% is found, which varies strongly as a function of the number of primary vertices. The overall trigger efficiency is calculated for each event depending on the lepton pseudorapidity and the primary vertex multiplicity. On average it is found to be 90.7%.

The tracking, muon identification, and single muon trigger efficiencies have been checked for possible dependences on the muon charge, p_{T}^{μ}, the azimuthal angle of the muon, η^{μ}, the pp primary vertex multiplicity, and on the data taking period. The only significant dependences seen are as a function of η^{μ} and, for the tracking efficiency alone, the primary vertex multiplicity. To account for the latter, the tag-and-probe sample used to determine the tracking efficiencies is reweighted such that it has the same primary vertex

multiplicity as the offline selected Z sample. The variation as a function of pseudorapidity is accounted for by performing the efficiency correction event-by-event as function of the pseudorapidities of the final state muons. The GEC efficiency correction is performed event-by-event as a function of the primary vertex multiplicity.

4.3 Corrections

The Z selection criteria define the fiducial region of the measurement. Simulated events are used to determine the acceptance $\mathcal{A}$ which accounts for migration into or out of the fiducial range of the measurement, due to resolution. The acceptance is estimated with simulated events. It is found to be consistent with unity.

The measured cross-sections are corrected to Born level in quantum electrodynamics (QED) in order to provide a consistent comparison with NLO and NNLO QCD predictions, which do not include the effects of FSR. Corrections have been estimated using Herwig++ [11] and cross-checked with Photos [12] interfaced to Pythia.

Pythia simulation is used to determine correction factors that account for bin-to-bin migrations due to resolution effects. With the exception of the first bin in Z boson p_{T}, all of the correction factors for each bin are compatible with unity. For the differential Z boson cross-section measurements presented here, these factors are used to perform a bin-to-bin correction accounting for resolution effects.

4.4 Luminosity

The absolute luminosity scale was measured at specific periods during the data taking, using both Van der Meer scans [13] where colliding beams are moved transversely across each other to determine the beam profile, and a beam-gas imaging method [14, 15]. Both methods give similar results and are estimated to have a precision of 3.5%. The knowledge of the absolute luminosity scale is used to calibrate the number of tracks in the VELO, which is found to be stable throughout the data-taking period and can therefore be used to monitor the instantaneous luminosity of the entire data sample. The dataset for this analysis corresponds to an integrated luminosity of $1.013 \pm 0.036\,\mathrm{fb}^{-1}$.

4.5 Systematic uncertainties

Aside from the uncertainty on the luminosity measurement, the main sources of experimental uncertainties come from the determination of the efficiencies and purity. The following sources have been considered:

1. **Efficiencies**: When added in quadrature, the uncertainties on the determination of the reconstruction and trigger efficiencies lead to a systematic uncertainty for the total cross-sections of 1.7%, where the largest components are due to the tracking and GEC efficiency determinations, which both contribute an uncertainty of 1.1%. The uncertainties on the tracking, muon identification and single muon trigger

Table 1: Contributions to the systematic uncertainty for the total Z cross-sections.

Source	Uncertainty (%)	Between bins
Tracking efficiency	± 1.1	mostly correlated
GEC efficiency	± 1.1	correlated
Muon-id efficiency	± 0.5	mostly correlated
Muon trigger efficiency	± 0.5	mostly correlated
Magnet polarity	± 1.6	uncorrelated
Bin-to-bin migrations	± 0.7	uncorrelated
FSR correction	± 0.2	uncorrelated
Signal purity	± 0.03	correlated
Total	± 2.5	
Luminosity	± 3.5	correlated

efficiencies have two contributions: the statistical uncertainty due to the sizes of the tag-and-probe samples, and the uncertainty due to the methods. The statistical uncertainties (0.5% for tracking, 0.1% for muon identification and trigger) are smaller than the uncertainties on the methods, which are estimated to be 1% [10], 0.5%, and 0.5% for the tracking, muon identification and single muon trigger efficiencies, respectively.

2. **Magnet polarity**: As a cross-check the full analysis has been performed separately using the two magnet polarity sub-datasets (magnet polarity up and magnet polarity down). Systematic differences are seen as a function of Z boson p_{T} and ϕ^*, with the largest discrepancies seen in the first bin in p_{T} and the last two bins in ϕ^*. Half of the observed difference is taken as an additional systematic uncertainty. On average this leads to a systematic uncertainty of 1.6%.

3. **Bin migration:** The statistical uncertainty on the determination of the bin-to-bin migration correction factors is taken as an additional uncertainty. On average this leads to a systematic uncertainty of 0.7%.

4. **FSR correction**: The uncertainty on the FSR correction is the quadratic sum of the statistical uncertainty from Herwig++ and the difference between the total corrections determined using Herwig++ and with Photos [16]. The uncertainty from this source is 0.2%.

5. **Purity**: The uncertainty on the determination of the sample purity leads to a 0.03% uncertainty on the total cross-section.

For the total cross-section measurement, the systematic uncertainties on each bin are combined by taking the uncertainties associated with the GEC, the luminosity, the signal purity, and the uncertainties on the tag-and-probe methods to be fully correlated between

bins. The correlations between the statistical uncertainties on the determination of the tracking, muon identification and single muon trigger efficiencies are determined using simulated $Z \to \mu\mu$ events. The other systematic uncertainties are taken to be uncorrelated between bins. The contributions to the uncertainty of the total cross-section are listed in table 1.

5 Results

The inclusive cross-section for $Z \to \mu\mu$ production for muons with $p_{\rm T}^{\mu} > 20\,{\rm GeV}/c$ in the pseudorapidity region $2.0 < \eta_{\mu} < 4.5$ and the invariant mass range $60 < M_{\mu\mu} < 120\,{\rm GeV}/c^2$ is measured to be

$$\sigma_{Z\to\mu\mu} = 75.4 \pm 0.3 \pm 1.9 \pm 2.6 \text{ pb},$$

where the first uncertainty is statistical, the second systematic and the third is due to the luminosity. The total cross-section is obtained by summing the contributions of the y bins, summing the ϕ^* or $p_{\rm T}$ bins gives very consistent results. This measurement agrees very well with the NNLO prediction by FEWZ (MSTW08 PDF set) of $74.7\ ^{+1.6}_{-1.4}\ ^{+0.4}_{-0.4}$ pb, where the first uncertainty is from the PDF uncertainty, evaluated at 68% CL and the second the theory uncertainty. The latter is estimated by varying the factorisation and renormalisation scales by a factor of two around the nominal value. Figure 2 shows a comparison of the measured total cross-section with the previous LHCb measurements in the electron and tau channels, and with the NNLO predictions from FEWZ.

The differential results are compared to theoretical predictions calculated at NNLO with the program FEWZ [17] (PDF sets of MSTW08 [18], NNPDF21 [19], CT10 [20], and ABM11). The scale uncertainties are estimated with FEWZ by varying the renormalisation and factorisation scales by factors of two around the nominal. The uncertainties for each set correspond to the PDF uncertainties at 68% and the scale uncertainties added in quadrature. Additionally, the results are compared to RESBOS [21] and to POWHEG [22]. Powheg provides a NLO calculation that is interfaced to the parton shower model from PYTHIA. For the POWHEG predictions, the effects of final state radiation are not included and only the statistical uncertainties are considered. The RESBOS[2] generator resums the leading contribution to next-to-next-to-leading logarithms and matches the result to an approximated NNLO QCD calculation. For the RESBOS calculations, the uncertainties from the PDFs, scale, and non-perturbative effects are considered.

The differential cross-sections are shown in Figs. 3-6. The measurements are compared to the NNLO predictions of FEWZ and to the predictions from RESBOS and POWHEG. The rapidity distribution is in very good agreement with all three predictions. The NNLO

[2]The P branch of RESBOS is used with grids for the LHC at $\sqrt{s} = 7$ TeV based on the CT10 PDF sets. The value of $\alpha_S(M_Z)$ used in the calculation is 0.118. The computation is performed by using the non-canonical combination [23] of the scale parameters that enter the Collins-Soper-Sterman resummation formalism: the choice for the coefcients is $C_1 = C_3 = 2 \cdot b_0$ and $C_2 = C_4 = 1/2$. The non-perturbative factor, a_1, in the Gaussian smearing function is set to $1.1\,{\rm GeV}^2$.

prediction fails to describe the shapes of the differential cross section as a function of ϕ^* and $p_{\rm T}$. Both these distributions are described reasonably well by RESBOS and POWHEG. The measurements as a function of Z boson rapidity and ϕ^* are also compared to the results from the LHCb $Z \to ee$ analysis [2], as shown in Fig. 7.

The measured cross section has been extrapolated to the fiducial volume of ATLAS in order to compare to their measurement [24]. The ATLAS measurement is based on 35 pb^{-1} of data taken in 2010. The measurements are performed in the electron and muon channel and are finally combined. The results are given for lepton $p_{\rm T} > 20\,{\rm GeV}/c$, Z boson rapidity $|y| < 3.6$ and invariant mass $66 < M_{\ell\ell} < 116\,{\rm GeV}/c^2$.

The extrapolation factors are calculated with FEWZ at NLO, the method is described in detail in [25]. Figure 8 shows the extrapolated LHCb cross sections for the measurement presented in this note as well as the measurement in the electron channel together with the ATLAS results. There is general agreement in the overlap region of the measurements, though the LHCb results tend to be slightly higher in the overlap region. This is in agreement with the observation that the ATLAS published results are slightly lower than the NNLO predictions in this region whereas the LHCb results are slightly higher.

The extrapolation factors are tabulated in Table 5, all the uncertainties considered for the determination of the factors are listed separately.

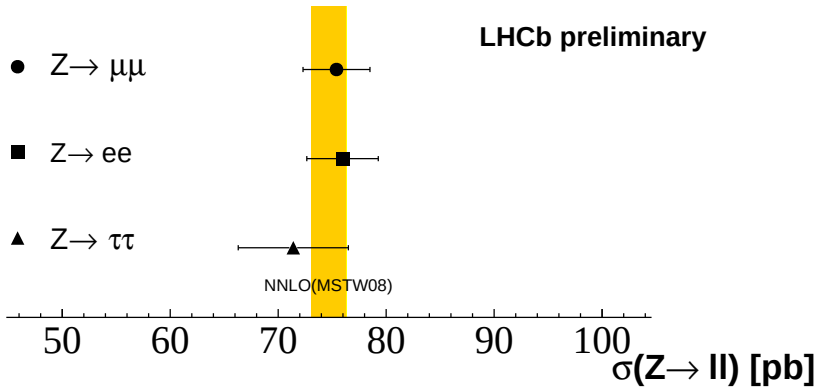

Figure 2: A comparison of the total $Z \to \mu\mu$ cross-section measured in this analysis with the $Z \to ee$ [2] and $Z \to \tau\tau$ [3] cross-sections measured at LHCb. The fixed order NNLO prediction from FEWZ using the MSTW08 PDF set is also shown.

6 Conclusions

A measurement of the cross-section for $Z \to \mu\mu$ production is presented using LHCb data recorded in 2011. The Z bosons are reconstructed from muons with a transverse momentum larger than 20 GeV/c in the pseudorapidity range $2.0 < \eta < 4.5$. The invariant mass of the dimuon system is restricted to $60 < M < 120$ GeV/c^2. The total cross-section in the fiducial range of the selection is found to be in excellent agreement with next-to-next-to leading order (NNLO) perturbative QCD calculations.

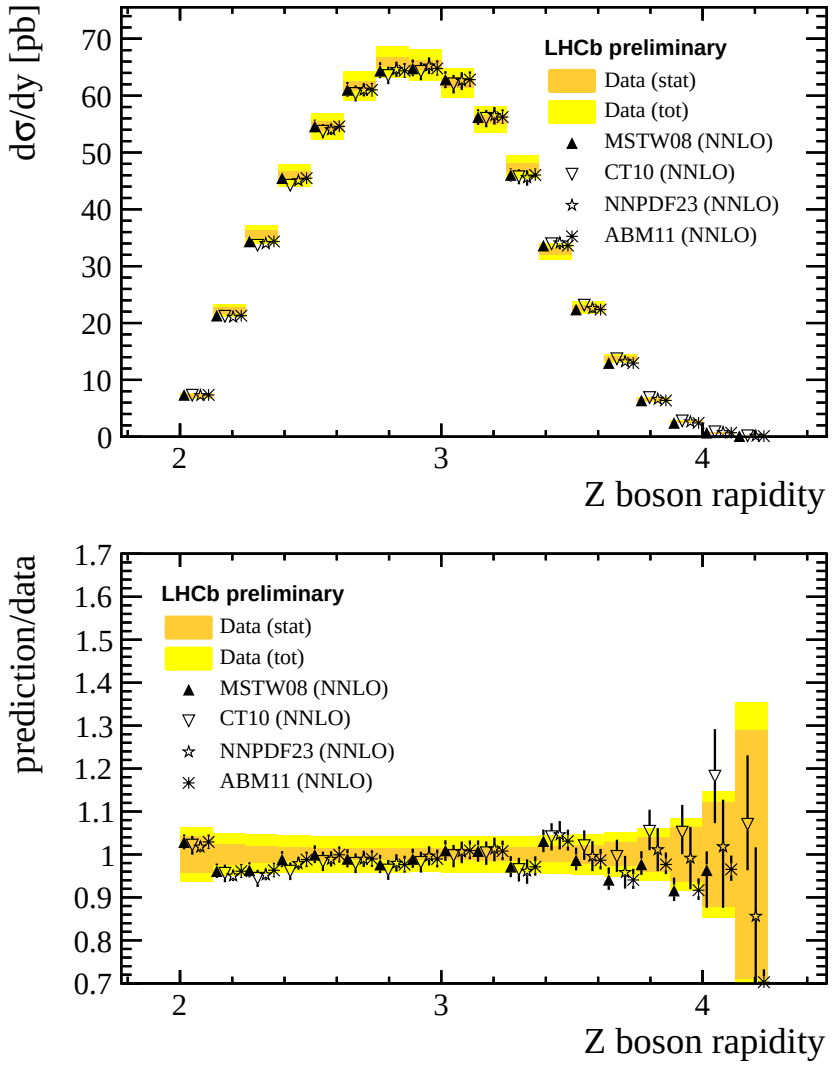

Figure 3: Top: Differential cross-section for $Z \to \mu\mu$ as a function of y of the Z boson. The dark shaded (orange) bands correspond to the statistical uncertainties, the light hatched (yellow) band to the statistical and systematic uncertainties added in quadrature. Superimposed are the fixed order NNLO predictions from FEWZ using the MSTW08, CT10 and NNPDF23 PDF sets. Bottom: ratio of the QCD predictions to data.

Differential cross sections as a function of the y, ϕ^* and p_{T} of the Z are compared to NNLO predictions as well as to predictions of RESBOS and POWHEG. The rapidity distribution is in very good agreement with all three predictions. The NNLO prediction fails to describe the shapes of the differential cross section as a function of ϕ^* and p_{T}. Both these distributions are described reasonably well by RESBOS and POWHEG.

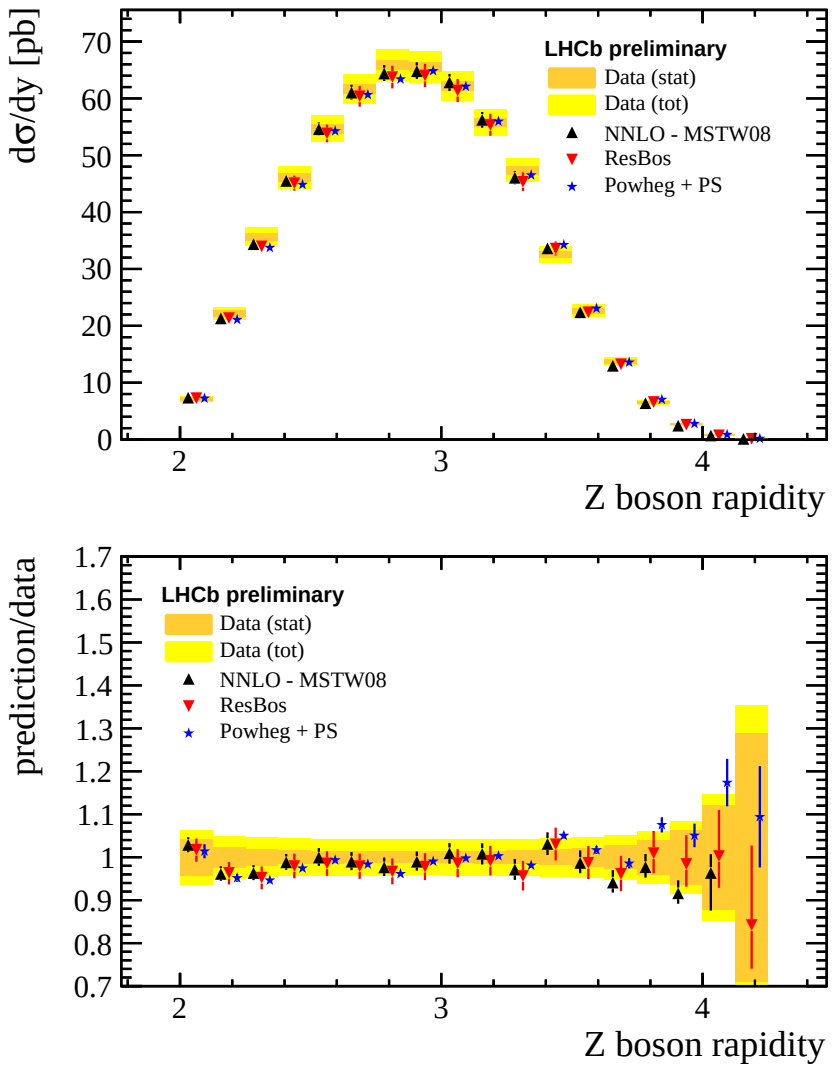

Figure 4: Top: Differential cross-section for $Z \to \mu\mu$ as a function of y of the Z boson. The dark shaded (orange) bands correspond to the statistical uncertainties, the light hatched (yellow) band to the statistical and systematic uncertainties added in quadrature. Superimposed are the predictions from FEWZ (NNLO), RESBOS and POWHEG. Bottom: ratio of the QCD predictions to data.

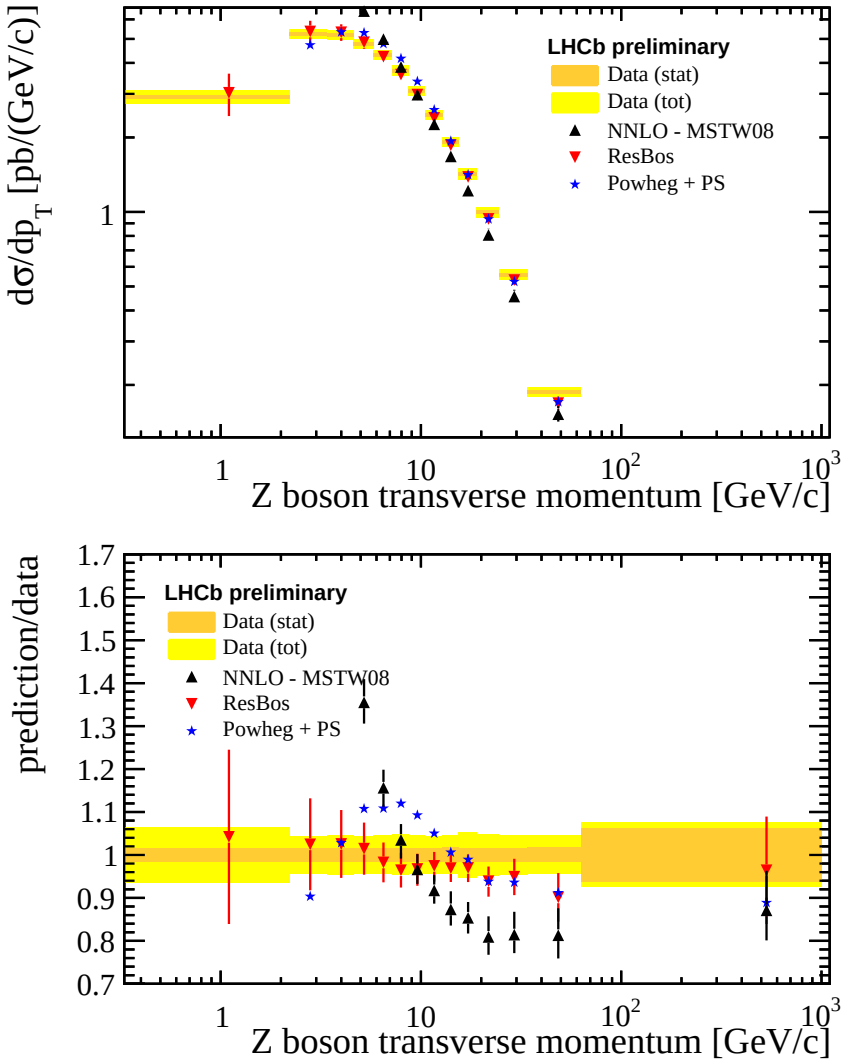

Figure 5: Top: Differential cross-section for $Z \to \mu\mu$ as a function of $p_{\rm T}$ of the Z boson. The dark shaded (orange) band corresponds to the statistical uncertainties, the light hatched (yellow) band to the statistical and systematic uncertainties added in quadrature. Superimposed are the predictions from FEWZ (NNLO), RESBOS and POWHEG. The differential cross section in the largest bin is very low and not displayed in the figure. Bottom: ratio of the QCD predictions to data.

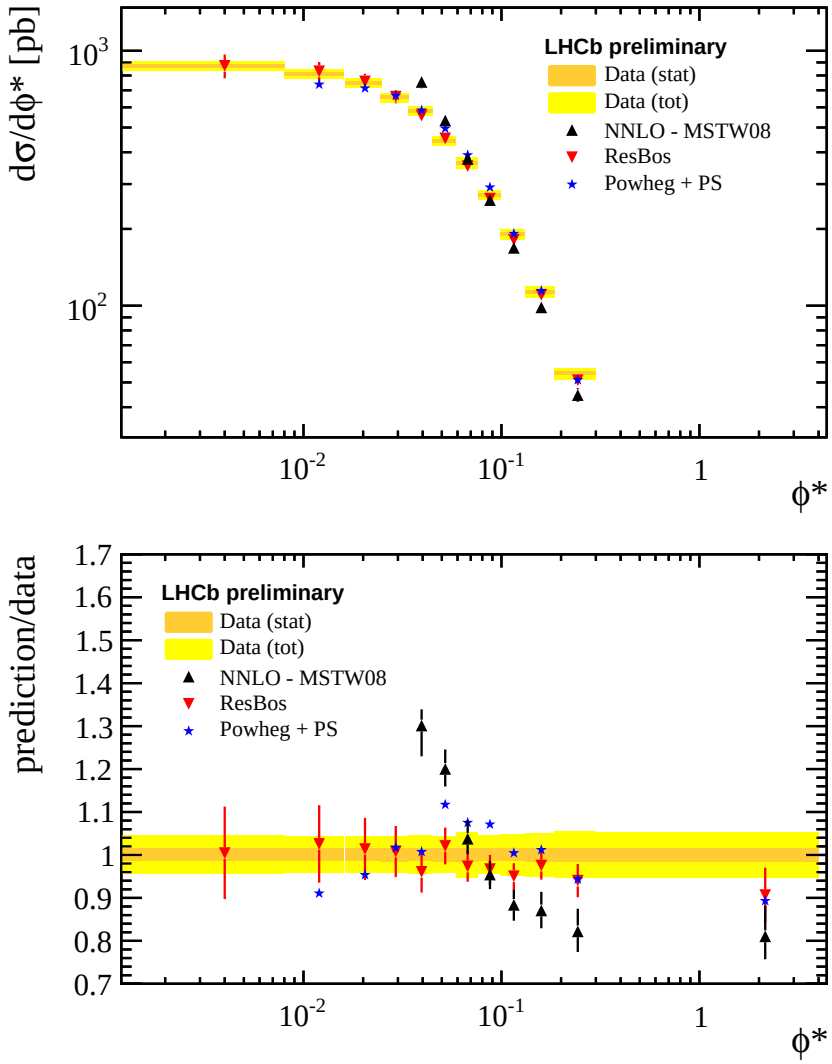

Figure 6: Top: Differential cross-section for $Z \to \mu\mu$ as a function of ϕ^* of the Z boson. The dark shaded (orange) band corresponds to the statistical uncertainties, the light hatched (yellow) band to the statistical and systematic uncertainties added in quadrature. Superimposed are the predictions from FEWZ (NNLO), RESBOS and POWHEG. The differential cross section in the largest bin is very low and not displayed in the figure. Bottom: ratio of the QCD predictions to data.

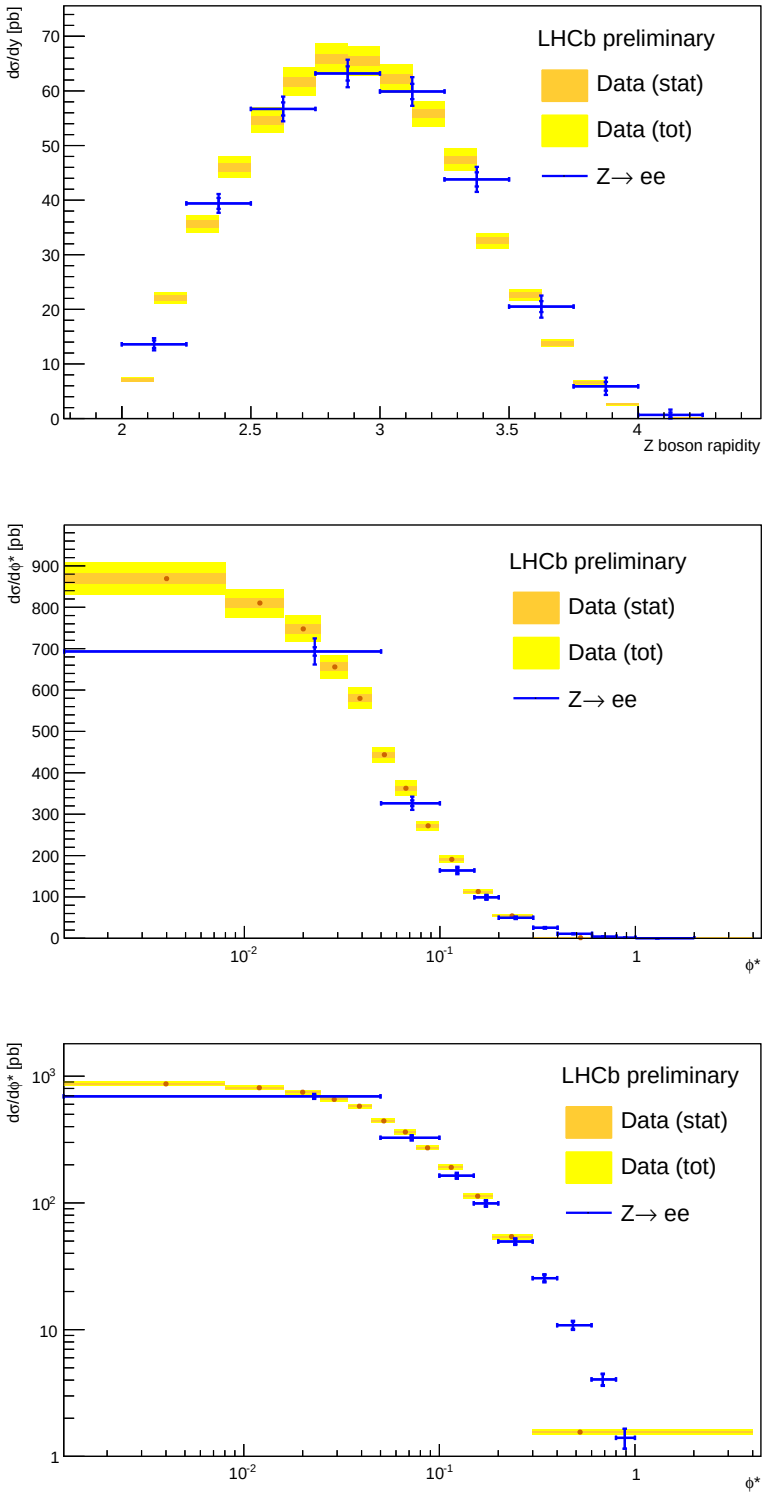

Figure 7: Comparison of the differential results as a function of the Z boson rapidity and ϕ^* with the values from the LHCb $Z \to ee$ measurement [2].

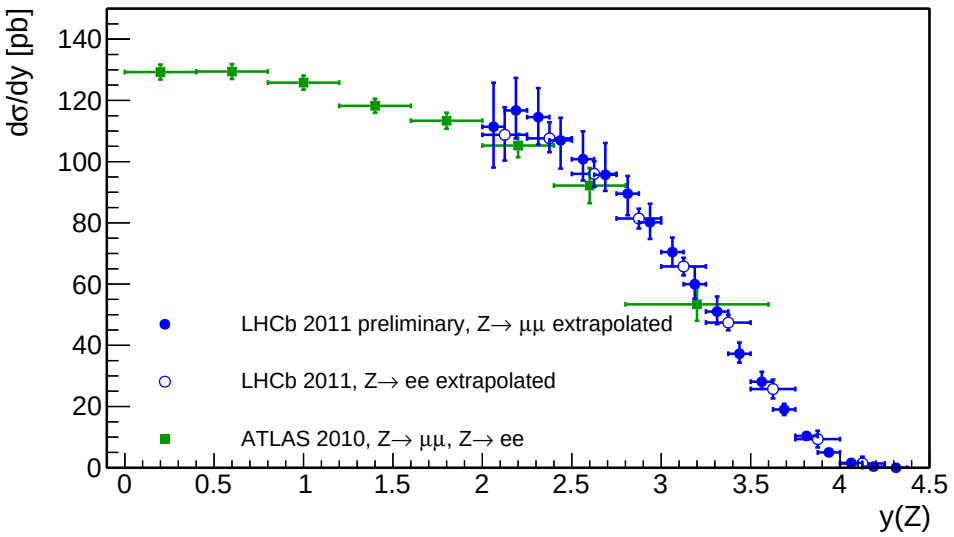

Figure 8: Differential cross-section for Z boson production as a function of the rapidity of the Z boson. The LHCb results in the muon (this note) and the electron [2] channels are extrapolated to the fiducial volume of the ATLAS measurement ($66 < M_{\ell\ell} < 116$ GeV/c^2, $p_{\rm T} > 20$ GeV/c) which is shown in green.

Table 2: Differential cross section $d\sigma/dy$ as a function of y of the Z.

y	$d\sigma/dy$ [pb]	stat [pb]	syst [pb]	lumi [pb]	Total [pb]
2.000 - 2.125	7.147	0.304	0.229	0.250	0.456
2.125 - 2.250	22.159	0.533	0.539	0.776	1.084
2.250 - 2.375	35.663	0.668	0.793	1.248	1.622
2.375 - 2.500	46.027	0.747	0.934	1.611	2.006
2.500 - 2.625	54.624	0.807	1.071	1.912	2.335
2.625 - 2.750	61.657	0.849	1.196	2.158	2.609
2.750 - 2.875	65.937	0.869	1.253	2.308	2.766
2.875 - 3.000	65.475	0.860	1.237	2.292	2.743
3.000 - 3.125	62.250	0.834	1.179	2.179	2.614
3.125 - 3.250	55.794	0.787	1.061	1.953	2.358
3.250 - 3.375	47.400	0.721	0.924	1.659	2.031
3.375 - 3.500	32.605	0.592	0.664	1.141	1.447
3.500 - 3.625	22.681	0.493	0.499	0.794	1.060
3.625 - 3.750	13.774	0.383	0.351	0.482	0.709
3.750 - 3.875	6.535	0.262	0.200	0.229	0.401
3.875 - 4.000	2.646	0.167	0.117	0.093	0.224
4.000 - 4.125	0.731	0.089	0.056	0.026	0.108
4.125 - 4.250	0.150	0.043	0.030	0.005	0.053

Table 3: Differential cross section $d\sigma/d\phi^*$ as a function of ϕ^* of the Z.

ϕ^*	$d\sigma/d\phi^*$ [pb]	stat [pb]	syst [pb]	lumi [pb]	Total [pb]
0.000 - 0.008	869.175	12.517	20.328	30.421	38.670
0.008 - 0.016	810.218	12.077	15.976	28.358	34.716
0.016 - 0.0245	747.675	11.258	14.320	26.169	31.884
0.0245 - 0.034	655.802	9.950	12.882	22.953	28.139
0.034 - 0.045	579.789	8.708	13.687	20.293	25.980
0.045 - 0.059	443.706	6.735	8.696	15.530	19.031
0.059 - 0.076	362.634	5.527	13.460	12.692	19.308
0.076 - 0.099	271.970	4.104	6.135	9.519	12.045
0.099 - 0.132	190.774	2.864	5.768	6.677	9.277
0.132 - 0.186	113.094	1.724	3.677	3.958	5.671
0.186 - 0.300	54.238	0.824	2.070	1.898	2.927
0.300 - 4.000	1.555	0.025	0.057	0.054	0.083

Table 4: Differential cross section $d\sigma/dp_{\mathrm{T}}$ as a function of p_{T} of the Z.

p_{T} [GeV/c]	$d\sigma/dp_{\mathrm{T}}$ [pb/(GeV/c)]	stat [pb/(GeV/c)]	syst [pb/(GeV/c)]	lumi [pb/(GeV/c)]	Total [pb/(GeV/c)]
0.000 - 2.200	2.908	0.046	0.150	0.102	0.187
2.200 - 3.400	5.230	0.081	0.105	0.183	0.226
3.400 - 4.600	5.187	0.079	0.131	0.182	0.238
4.600 - 5.800	4.780	0.075	0.102	0.167	0.210
5.800 - 7.200	4.315	0.066	0.098	0.151	0.192
7.200 - 8.700	3.722	0.059	0.102	0.130	0.175
8.700 - 10.500	3.081	0.049	0.069	0.108	0.137
10.500 - 12.800	2.463	0.038	0.051	0.086	0.107
12.800 - 15.400	1.920	0.031	0.042	0.067	0.085
15.400 - 19.000	1.428	0.023	0.053	0.050	0.076
19.000 - 24.500	0.998	0.016	0.030	0.035	0.049
24.500 - 34.000	0.559	0.009	0.015	0.020	0.026
34.000 - 63.000	0.187	0.003	0.004	0.007	0.008
63.000 - 1000.000	0.0016	0.0001	0.000	0.000	0.00012

Table 5: Extrapolation to the ATLAS fiducial volume ($66 < M_{\ell\ell} < 116$ GeV/c^2, no cut on η). These correction factors must be applied to the measured cross section to get the extrapolated cross section. The positive and negative uncertainties are labeled "up" and "down", respectively.

y	C_i	Stat.	PDF		PDF set		Theory		Model	Total	
			up	down	up	down	up	down		up	down
2.000 - 2.125	15.798	0.073	0.026	0.027	0.094	0.1	0.345	0.019	0.0001	0.368	0.134
2.125 - 2.250	5.354	0.011	0.008	0.009	0.012	0.01	0.069	0.038	0.021	0.074	0.047
2.250 - 2.375	3.265	0.005	0.004	0.005	0.009	0.009	0.03	0.026	0.001	0.032	0.029
2.375 - 2.500	2.358	0.004	0.003	0.003	0.003	0.003	0.013	0.021	0.0001	0.015	0.022
2.500 - 2.625	1.865	0.003	0.002	0.002	0.002	0.003	0.016	0.01	0.001	0.016	0.011
2.625 - 2.750	1.564	0.002	0.001	0.001	0.004	0.004	0.016	0.005	0.002	0.017	0.007
2.750 - 2.875	1.367	0.002	0.001	0.001	0.004	0.003	0.005	0.011	0.0001	0.007	0.012
2.875 - 3.000	1.226	0.002	0.001	0.001	0.001	0.002	0.009	0.003	0.0001	0.01	0.005
3.000 - 3.125	1.128	0.002	0.001	0.001	0.004	0.002	0.006	0.003	0.001	0.008	0.005
3.125 - 3.250	1.065	0.002	0.0001	0.0001	0.001	0.001	0.002	0.004	0.001	0.003	0.005
3.250 - 3.375	1.063	0.002	0.0001	0.0001	0.004	0.004	0.005	0.005	0.0001	0.008	0.008
3.375 - 3.500	1.123	0.003	0.001	0.001	0.004	0.002	0.011	0.004	0.005	0.013	0.007
3.500 - 3.625	1.216	0.003	0.001	0.001	0.004	0.002	0.01	0.002	0.0001	0.012	0.006
3.625 - 3.750	1.353	0.005	0.002	0.002	0.002	0.001	0.009	0.016	0.004	0.011	0.018
3.750 - 3.875	1.537	0.007	0.003	0.003	0.005	0.006	0.012	0.006	0.015	0.021	0.019
3.875 - 4.000	1.789	0.009	0.005	0.007	0.017	0.033	0.022	0.003	0.017	0.034	0.039
4.000 - 4.125	2.067	0.015	0.011	0.027	0.034	0.032	0.015	0.002	0.0001	0.052	0.055
4.125 - 4.250	2.25	0.031	0.031	0.121	0.14	0.116	0.04	0.001	0.127	0.198	0.213

References

[1] LHCb collaboration, R. Aaij *et al.*, *Inclusive W and Z production in the forward region at $\sqrt{s} = 7$ TeV*, JHEP **06** (2012) 058, arXiv:1204.1620.

[2] LHCb collaboration, R. Aaij *et al.*, *Measurement of the cross-section for $Z \to e^+e^-$ production in pp collisions at $\sqrt{s} = 7$ TeV*, JHEP **02** (2013) 106, arXiv:1212.4620.

[3] LHCb collaboration, R. Aaij *et al.*, *A study of the Z production cross-section in pp collisions at $\sqrt{s} = 7$ TeV using tau final states*, JHEP **01** (2013) 111, arXiv:1210.6289.

[4] A. Banfi *et al.*, *Optimisation of variables for studying dilepton transverse momentum distributions at hadron colliders*, Eur. Phys. J. **C71** (2011) 1600, arXiv:1009.1580.

[5] LHCb collaboration, A. A. Alves Jr. *et al.*, *The LHCb detector at the LHC*, JINST **3** (2008) S08005.

[6] T. Sjöstrand, S. Mrenna, and P. Skands, *PYTHIA 6.4 physics and manual*, JHEP **05** (2006) 026, arXiv:hep-ph/0603175.

[7] I. Belyaev *et al.*, *Handling of the generation of primary events in* Gauss*, the LHCb simulation framework*, Nuclear Science Symposium Conference Record (NSS/MIC) **IEEE** (2010) 1155.

[8] P. M. Nadolsky *et al.*, *Implications of CTEQ global analysis for collider observables*, Phys. Rev. **D78** (2008) 013004, arXiv:0802.0007.

[9] M. Cacciari *et al.*, *The anti-kt jet clustering algorithm*, JHEP **04** (2008) 063, arXiv:0802.1189.

[10] A. Jaeger, P. Seyfert, M. De Cian, J. van Tilburg and S. Hansmann-Menzemer, *A measurement of the track finding efficiency*, LHCb-PUB-2011-025 (2012).

[11] M. Bahr *et al.*, *Herwig++ physics and manual*, Eur. Phys. J. **C58** (2008) 639, arXiv:0803.0883.

[12] P. Golonka and Z. Was, *PHOTOS Monte Carlo: a precision tool for QED corrections in Z and W decays*, Eur. Phys. J. **C45** (2006) 97, arXiv:hep-ph/0506026.

[13] S. van der Meer, *Calibration of the effective beam height in the ISR*, ISR-PO/68-31, 1968.

[14] M. Ferro-Luzzi, *Proposal for an absolute luminosity determination in colliding beam experiments using vertex detection of beam-gas interactions*, Nucl. Instrum. Meth. **A553** (2005) 388.

[15] LHCb collaboration, R. Aaij *et al.*, *Absolute luminosity measurements with the LHCb detector at the LHC*, JINST **7** (2012) P01010, arXiv:1110.2866.

[16] K. Hamilton, *Private communication.*

[17] R. Gavin, Y. Li, F. Petriello, and S. Quackenbush, *FEWZ 2.0: A code for hadronic Z production at next-to-next-to-leading order*, Comput. Phys. Commun. **182** (2011) 2388, arXiv:1011.3540.

[18] A. D. Martin, W. J. Stirling, R. S. Thorne, and G. Watt, *Parton distributions for the LHC*, Eur. Phys. J. **C63** (2009) 189, arXiv:0901.0002.

[19] R. D. Ball *et al.*, *A first unbiased global NLO determination of parton distributions and their uncertainties*, Nucl. Phys. **B838** (2010) 136, arXiv:1002.4407.

[20] J. G. et. al., *The CT10 NNLO Global Analysis of QCD*, arXiv:1302.6246.

[21] G. A. Ladinsky and C.-P. Yuan, *The nonperturbative regime in QCD resummation for gauge boson production at hadron colliders*, Phys. Rev. **D50** (1994) 4239, arXiv:hep-ph/9311341; C. Balazs and C.-P. Yuan, *Soft gluon effects on lepton pairs at hadron colliders*, Phys. Rev. **D56** (1997) 5558, arXiv:hep-ph/9704258; F. Landry, R. Brock, P. M. Nadolsky, and C.-P. Yuan, *Tevatron Run-1 Z boson data and Collins-Soper-Sterman resummation formalism*, Phys. Rev. **D67** (2003) 073016, arXiv:hep-ph/0212159.

[22] P. Nason, *A new method for combining NLO QCD with shower Monte Carlo algorithms*, JHEP **11** (2004) 040, arXiv:hep-ph/0409146; S. Frixione, P. Nason, and C. Oleari, *Matching NLO QCD computations with parton shower simulations: the POWHEG method*, JHEP **11** (2007) 070, arXiv:0709.2092; S. Alioli, P. Nason, C. Oleari, and E. Re, *A general framework for implementing NLO calculations in shower Monte Carlo programs: the POWHEG BOX*, JHEP **06** (2010) 043, arXiv:1002.2581.

[23] M. Guzzi and P. M. Nadolsky, *Non-perturbative contributions to a re-summed leptonic angular distribution in inclusive Z/gamma boson production*, arXiv:1209.1252.

[24] ATLAS collaboration, G. Aad *et al.*, *Measurement of the $W \to l\nu$ and $Z/\gamma^* \to ll$ production cross sections in proton-proton collisions at $\sqrt{s} = 7$ TeV with the ATLAS detector*, JHEP **12** (2010) 060, arXiv:1010.2130.

[25] LHCb collaboration, R. Aaij *et al.*, *Graphical comparison of the LHCb measurements of W and Z boson production with ATLAS and CMS*, LHCb-CONF-2013-005.